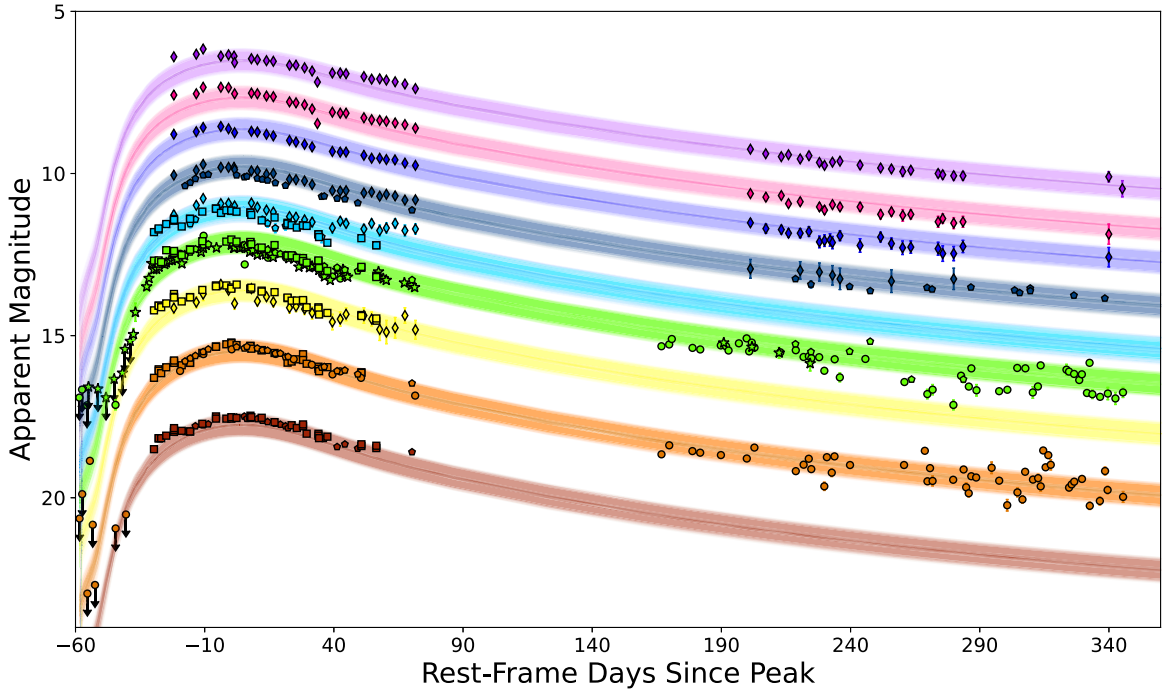

Figure 6. MOSFiT nested sampling fits to AT 2019azh photometry. Solid lines represent the medians of samples of light curves, while the shaded regions indicate the variance within each sample of models. Overall, the ensembles of models provide a reasonably good fit to the photometric data, but the best-fit parameters are not fully self-consistent (see Section 4.6). Arrows indicate 3σ nondetection upper limits. Colors, markers, and offsets are the same as in Figure 1.

compare these results to those found through MOSFiT in Section 4, though we do not expect them to agree since each model assumes a different emission mechanism responsible for the observed light curve.

3.2. Spectroscopy

3.2.1. Coronal Emission Lines

We use a custom analysis code (Clark et al. 2024, in preparation) to check for the presence of narrow [Fe VII], [Fe X], [Fe XI], and [Fe XIV] coronal emission lines in our spectra. Such lines are seen in extreme coronal line emitters (e.g., Komossa et al. 2008; Wang et al. 2012; Yang et al. 2013), a subset of which is associated with TDEs (e.g., Onori et al. 2022; Short et al. 2023; Callow et al. 2024; Clark et al. 2024) occurring in gas-rich environments. We find no significant evidence for such features in any of our spectra.

3.2.2. Other Emission Lines

To identify and study the broad emission lines, we follow the spectral analysis process outlined by Charalampopoulos et al. (2022) for removing host galaxy and continuum contributions to the emission line profiles (after performing the photometric calibration and Galactic extinction correction as detailed in Section 2). We exclude from this analysis the du Pont spectra to avoid telluric contamination, and all spectra taken after the seasonal gap (day 205 after peak and onward) given that the broad emission lines are very weak at such late times.

First, we subtract the host galaxy spectrum from each TDE spectrum after resampling the host spectrum to the wavelengths of the TDE spectrum using the SciPy interp1d function.[58] Since different spectra are taken under different seeing conditions, and the TDE spectra are taken with varying slit widths and angles, while the SDSS host spectrum was obtained through a fiber, there will be different host galaxy contributions to each TDE spectrum. Thus, it is impossible to completely remove host galaxy emission from the TDE spectra. Here, we attempt to minimize host galaxy contamination, but some residuals likely remain (see below).

Next, we identify line-free regions in the host-subtracted spectra to fit and remove the spectral continuum using a third-order polynomial. We use the line-free regions outlined by Charalampopoulos et al. (2022) as a basis, while tailoring them to match the AT 2019azh spectra. The selected line-free rest-frame wavelength ranges are 3900–4000, 4220–4280, 5100–5550, 6000–6100, and 6800–7000 Å.

An example of this spectral processing procedure, as performed on the spectrum from 13 days after peak brightness, is provided in Figure E1 in Appendix E. All spectra after host and continuum removal, for which this process was conducted, are presented in Figure E2 in Appendix E.

Broad emission lines of Hα, He II λ4686, and He I λ5876 are evident, as in other UV/optical TDEs (e.g., Gezari et al. 2012; Arcavi et al. 2014; Holoien et al. 2016b). The broad He II λ4686 emission line appears already in the first spectrum, remains relatively strong and broad until the seasonal gap at 72 days after the light-curve peak, and weakens in the spectra obtained after the gap (see Figure E2 in Appendix E). The broad Hα emission line strengthens at early times and later significantly weakens and narrows in the post-seasonal gap spectra. This behavior was observed in some other TDEs (e.g., Gezari et al. 2012; Holoien et al. 2014b, 2016b), and is discussed further in Section 3.2.3.

In addition to the broad emission lines, narrow Balmer Hβ and Hγ emission lines are seen in the host- and continuum-subtracted spectra. These lines likely originate from

[58] https://docs.scipy.org/doc/scipy/reference/generated/scipy.interpolate.interp1d.html

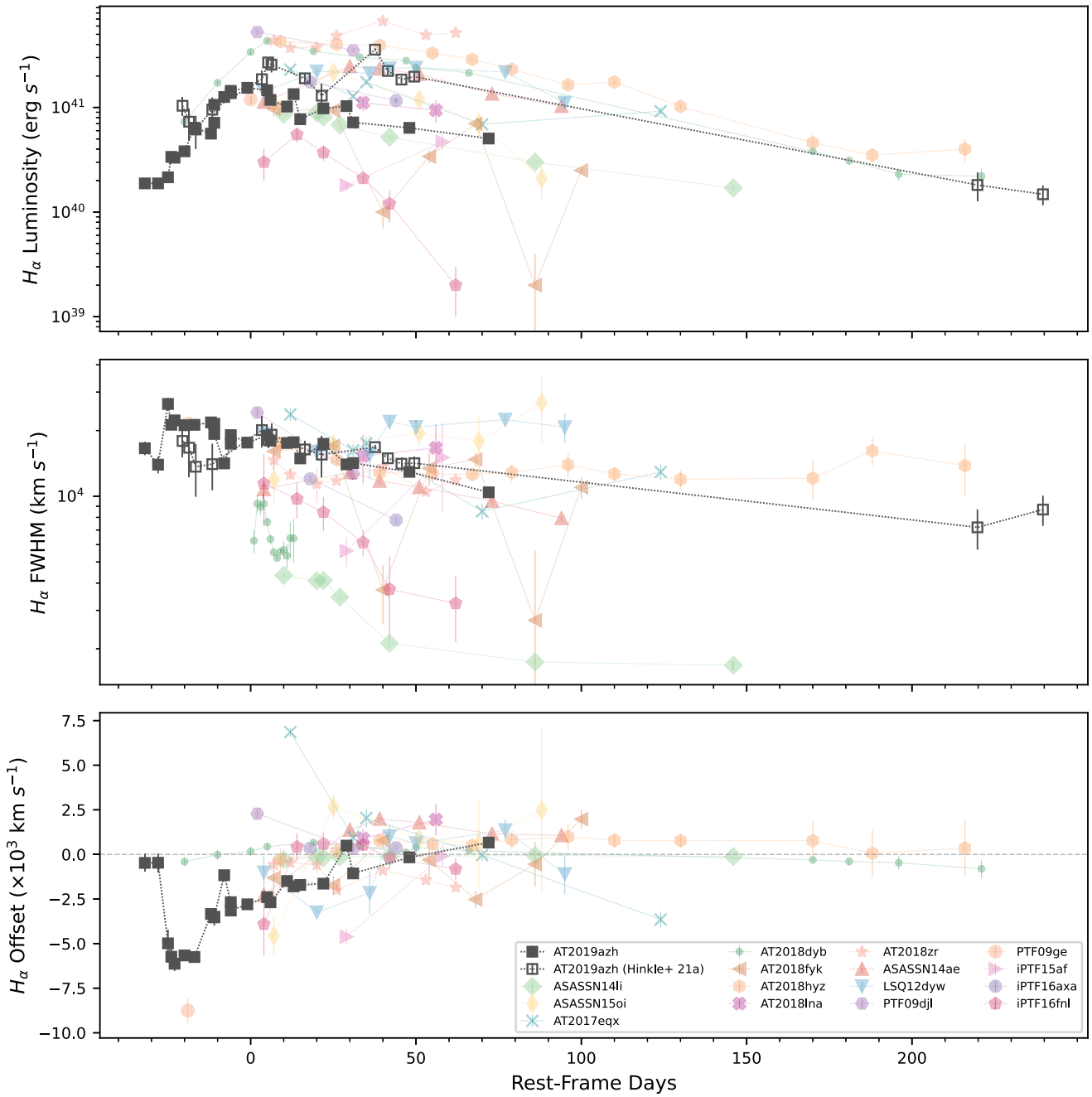

Figure 7. Evolution of Hα line luminosity (top), FWHM (center), and central wavelength offset (bottom) of AT 2019azh from this work compared to those of Hinkle et al. (2021a) and a sample of 15 TDEs from Charalampopoulos et al. (2022). AT 2019azh is plotted relative to its *g*-band peak, while the comparison data are plotted relative to their peak or discovery date (see Charalampopoulos et al. 2022, for details).

(The data used to create this figure are available.)

oversubtraction of the host galaxy spectrum (as they also appear in the SDSS host spectrum as narrow absorption lines; see Figure 2). We also find a strong, narrow [O III] λ5007 absorption line in the host-subtracted spectra (see Figure E1 in Appendix E), which is probably also an oversubtracted host galaxy emission line.

3.2.3. Hα Line Evolution

Following Charalampopoulos et al. (2022), we quantify the evolution of the Hα emission line, as it is a relatively isolated line. For each host- and continuum-subtracted spectrum, we fit the Hα emission line with a Gaussian using the nonlinear least-squares method of the `LMFIT`[59] package. We use the same initial guesses for the center (6563 Å) and width (150 Å, corresponding to a Doppler velocity of $\sim$10,000 km s^{-1}), for all spectra. All Gaussian fits, after normalizing the peak of the feature, are shown in Figure E3 in Appendix E.

The evolution of the Hα line luminosity is presented in the top panel of Figure 7, along with data from 15 other TDEs obtained from Charalampopoulos et al. (2022), which were measured using

[59] https://lmfit.github.io/lmfit-py/

Table 6
Hα Luminosity, FWHM, and Central Wavelength Offset of AT 2019azh

Phase	Hα Luminosity (10^{40} erg s^{-1})	Hα FWHM (km s^{-1})	Hα Central Wavelength Offset (km s^{-1})
−32	1.88 ± 0.17	16589.22 ± 1171.02	−475.83 ± 487.42
−28	1.88 ± 0.21	13954.00 ± 1231.55	−466.12 ± 522.95
−25	2.15 ± 0.18	26471.07 ± 1809.76	−4986.51 ± 768.48
−24	3.37 ± 0.21	21255.54 ± 1000.60	−5735.38 ± 424.88
−23	3.31 ± 0.19	22257.40 ± 963.45	−6126.03 ± 409.11
−20	3.81 ± 0.14	21156.45 ± 584.78	−5662.58 ± 248.32
−17	6.40 ± 0.28	21238.53 ± 717.22	−5751.50 ± 304.55
−12	5.62 ± 0.23	21790.47 ± 693.67	−3340.03 ± 294.55
−11	7.14 ± 0.46	21490.06 ± 1090.57	−3528.82 ± 463.09
−11	10.59 ± 0.23	19292.27 ± 319.33	−3488.98 ± 135.60
−8	12.63 ± 0.16	14136.78 ± 136.217	−1165.36 ± 57.84
−6	14.45 ± 0.36	17393.32 ± 347.60	−3145.95 ± 147.60
−6	13.69 ± 0.31	19052.18 ± 330.17	−2678.93 ± 140.20
−1	15.43 ± 0.31	17610.98 ± 269.39	−2797.66 ± 114.39
+5	14.56 ± 0.20	18962.47 ± 200.04	−2396.22 ± 84.94
+6	11.84 ± 0.14	17968.18 ± 162.57	−2685.32 ± 69.03
+11	10.18 ± 0.15	17536.29 ± 199.07	−1490.40 ± 84.53
+13	13.39 ± 0.16	17677.46 ± 157.96	−1792.32 ± 67.07
+15	7.72 ± 0.19	14905.48 ± 286.30	−1711.47 ± 121.57
+22	9.80 ± 0.10	17390.90 ± 141.47	−1640.46 ± 60.07
+29	10.26 ± 0.45	13992.84 ± 465.88	491.88 ± 197.83
+31	7.19 ± 0.08	14193.45 ± 124.82	−1065.69 ± 53.00
+48	6.38 ± 0.06	12932.58 ± 95.83	−166.10 ± 40.69
+72	5.05 ± 0.11	10420.17 ± 167.85	664.59 ± 71.28

Note. Phases are given relative to the *g*-band peak brightness.

the same methodology as described here and which constitute the largest sample of homogeneously analyzed TDE spectra to date. Around peak brightness, the Hα luminosity is similar to that of the comparison sample. The post-peak slight decay of the Hα luminosity is also consistent with the rest of the sample. However, the extensive pre-peak spectral observations of AT 2019azh reveal the initial formation of this emission line in a TDE for the first time. These observations can be used to constrain future models of spectral line formation in TDEs. We also compare our results with those of Hinkle et al. (2021a), which agree at early times but not at late times. This might be due to the different analysis method used by Hinkle et al. (2021a), where, for example, the continuum is removed differently than here.

We also measure the evolution of the full width at half-maximum (FWHM) intensity of the Gaussian fits to the Hα emission line of AT 2019azh, and compare them to those of the Charalampopoulos et al. (2022) sample and to the results of Hinkle et al. (2021a) in the middle panel of Figure 7. The FWHM of the Hα emission line of AT 2019azh is at the upper range of the Charalampopoulos et al. (2022) sample, and it shows a clear gradual decline. Here, our results are consistent with those of Hinkle et al. (2021a).

Finally, in the bottom panel of Figure 7, we compare the evolution of the Hα best-fit Gaussian central wavelength offset from the rest wavelength with that of the same sample from Charalampopoulos et al. (2022). While the line centers of the first two spectra are consistent with zero offset, a blueshift rapidly develops and slowly returns back to zero offset within a few months. The magnitude of the offset is consistent with those of other events in the Charalampopoulos et al. (2022) sample, but AT 2019azh is the only event showing this kind of evolution. In addition, from Figure 7, it appears that there is an anticorrelation

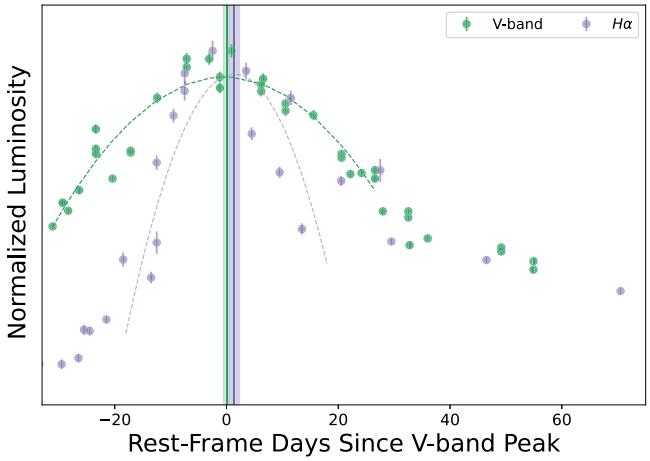

Figure 8. Hα luminosity evolution (purple), compared to the *V*-band light curve of AT 2019azh (green). The colored dashed lines are the parabolic fits to the data around peak brightness, from which the peak times were determined. The vertical solid lines and shaded regions mark the peak times for the *V*-band and Hα peaks, and their 1σ uncertainties, respectively. The Hα peak time is consistent with that of the *V*-band peak.

between the Hα FWHM and offset. Indeed, we find such an anticorrelation (with a Pearson coefficient of −0.876; see Figure E4 in Appendix E). However, events in the Charalampopoulos et al. (2022) sample do not show similar behavior, therefore this anticorrelation does not seem like a universal property of TDEs.

The Hα luminosity, FWHM, and central wavelength offset values for AT 2019azh are presented in Table 6.

Charalampopoulos et al. (2022) showed that TDEs exhibit a time lag between their light curve (i.e., continuum emission) and Hα luminosity peaks. Figure 8 compares the evolution of the Hα luminosity and the *V*-band light curve for AT 2019azh. To determine the peak time of the Hα line luminosity for AT 2019azh, we fit a second-order polynomial to the Hα luminosity from −18 to +18 days since the *g*-band peak and find that the peak occurred on MJD 58569.59 ± 1.07, or $\Delta t = 1.40 \pm 0.93$ days after the *V*-band light-curve peak.

4. Discussion

4.1. Spectroscopic Classification of AT 2019azh

In Figure 9 we compare the continuum-subtracted spectra around the peak of AT 2019azh to those of the Bowen TDE AT 2018dyb (Leloudas et al. 2019), the H+He-TDE AT 2020wey (Charalampopoulos et al. 2023), which also showed a possible early light-curve bump, and AT 2019ahk (Holoien et al. 2019b), which does not show such structure despite having a very densely sampled early-time light curve (see below).[60] AT 2019azh does not show N III λλ4100, 4640 emission like those seen in AT 2018dyb, meaning it is not a Bowen TDE. Its broad H and He II λ4686 emission features are similar to those of AT 2020wey, making it a H+He-TDE. AT 2019ahk shows strong AGN-like narrow spectral emission lines, not seen in most TDEs, implying it might be a different type of flare.

4.2. Peak Luminosity Time Delays

In Section 3.1.1, we measured a time delay in the peak luminosity between the different bands, with the redder bands

[60] We subtract the continuum of each spectrum following the procedure detailed in Section 3.2.2.

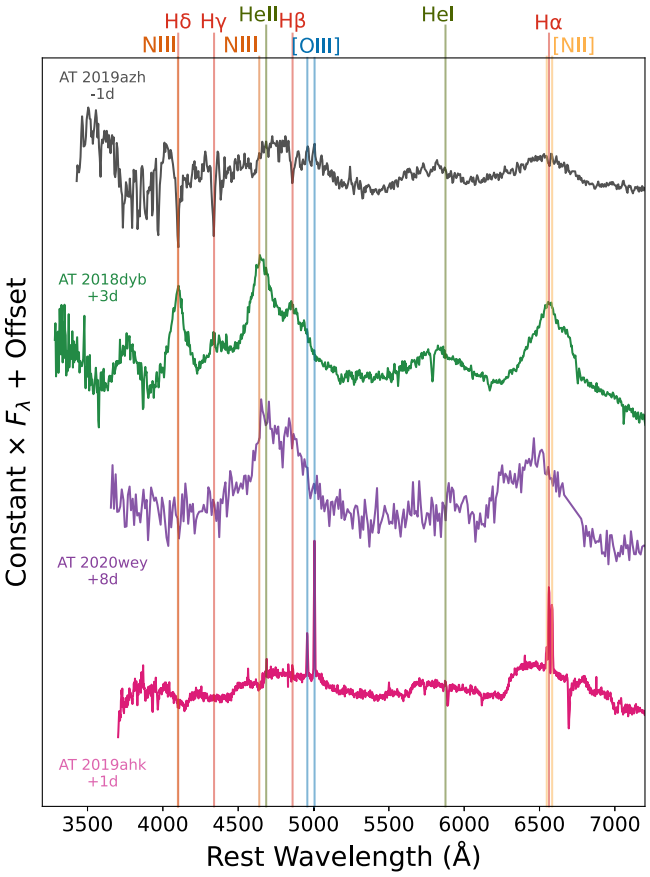

Figure 9. Spectral comparison around peak luminosity of AT 2019azh (host-subtracted spectrum) with the well-observed Bowen TDE AT 2018dyb (Leloudas et al. 2019, not host subtracted), the H+He-TDE AT 2020wey (Charalampopoulos et al. 2023, host subtracted), which also showed possible early light-curve structure, and AT 2019ahk (Holoien et al. 2019b, not host subtracted), which did not show such structure in its very densely sampled light-curve rise. All spectra are continuum-subtracted. The similarity of the AT 2019azh spectrum to that of AT 2020wey classifies it as a H+He-TDE. The spectrum of AT 2019ahk displays distinctive narrow emission lines, implying it might be an AGN-related flare rather than a *classical* TDE. Days relative to the light-curve peak are shown next to each spectrum.

peaking later than the bluer ones (Figure 3). Such behavior has been seen in other TDEs, such as AT 2018zr (PS18kh; Holoien et al. 2019a), AT 2019ahk (ASASSN-19bt; Holoien et al. 2019b), and AT 2018dyb (ASASSN-18pg; Holoien et al. 2020), where it has been attributed to the blackbody temperature evolution around the peak. Wang et al. (2023) also find that the optical emission lags behind the UV emission in the peculiar nuclear transient AT 2019avd. They interpret this lag as evidence for the optical emission being reprocessed UV emission. This phenomenon is also observed in AGNs (e.g., Shappee et al. 2014), where it is attributed to an accretion disk emission model (e.g., Cackett et al. 2007), according to which the inner, hotter accretion disk is illuminated by X-rays first, with the illumination progressing outward, causing variations in the light curve to manifest initially in the bluer bands associated with the inner disk, followed by the redder bands. An opposite time delay was measured for the TDE ASASSN-14li by Pasham et al. (2017). There, the UV lagging behind the optical is interpreted as evidence for the stream collision scenario.

4.3. Early Light-curve Structure

Our high-cadence photometric observations also reveal, for the first time, both a change in light-curve slope and a possible bump in the rising light curve of a TDE. The most densely sampled rising light curve of a TDE is that of AT 2019ahk (ASASSN-19bt; Holoien et al. 2019b), which was observed with a 30 minute cadence using TESS. Its light-curve rise is smooth (Figure 10), in stark contrast to that of AT 2019azh. However, AT 2019ahk might not be a spectroscopically *classical* TDE. As mentioned, it stands out in Figure 9 owing to its strong and narrow [O III] $\lambda\lambda$4959, 5007 and [N II] $\lambda\lambda$6548, 6584 emission lines, not commonly seen in TDE spectra. Furthermore, the host galaxy of AT 2019ahk is in the Seyfert region of the Baldwin–Phillips–Terlevich (Baldwin et al. 1981) diagram (see Figure 2 in Holoien et al. 2019b), indicating the presence of an AGN as an ionizing source. AT 2019ahk might thus be related to an AGN flare rather than a typical optical/UV TDE.

ASASSN-14ko (Holoien et al. 2014a) is another nuclear transient with a bump reported in its rising phase (Huang et al. 2023). However, it displays spectra more similar to those of AGNs (Payne et al. 2021) and periodicity in its outbursts (Payne et al. 2021, 2022, 2023), which are not seen in the class of TDEs to which AT 2019azh belongs. Hence, we do not consider it further here.

AT 2020wey, on the other hand, is a classical spectroscopically classified TDE (Figure 9), which does show a possible bump in its early *g*- and *r*-band light curves (Figure 10; Charalampopoulos et al. 2023). Unfortunately, this part of the light curve of AT 2020wey was not observed at a sufficiently high cadence to robustly characterize this feature. Finally, AT 2020zso is a TDE, which shows an abrupt change in its light-curve rise slope (Figure 10; photometry taken from Wevers et al. 2022).

No TDE emission model predicts specific light-curve features such as these. This could point toward the presence of more than one emission source as responsible for the UV/optical TDE emission. The photometry presented here could be used to test future TDE emission models.

4.4. Estimates of the SMBH Mass

Wevers (2020) derived the SMBH mass of the host of AT 2019azh using the M–σ relation from Gültekin et al. (2009a) with the velocity dispersion measured from the WHT spectrum presented here. They find an SMBH mass of $M_{\rm BH} = 2.29 \pm 2.27 \times 10^6\,M_\odot$. This mass is consistent with that found by `TDEMass` but is a factor of $\sim$7 smaller than that found by `MOSFiT`. We do not consider this definitive evidence favoring one model or the other since the host-galaxy-derived SMBH mass strongly depends on the choice of scaling relation and the spectral resolution used to infer the velocity dispersion, as is evident in the comparison to other works.

We present a summary of SMBH mass estimates obtained here and in other works using the two light-curve models and host galaxy scaling relations, along with the corresponding Eddington ratios for the peak bolometric luminosity, in Table 7. Our results are consistent with those of Hammerstein et al. (2023) for the `TDEMass` estimates, and marginally consistent (at the $\lesssim 2\sigma$ level) with the MOSFiT estimates from that work. Our results are not consistent with those of Hinkle et al. (2021a) or Nicholl et al. (2022). The discrepancy with

Table 7
SMBH Mass Estimates and Corresponding Eddington Ratios for the Peak Bolometric Luminosity

References	TDEMass		MOSFiT		Host Galaxy	
	$M_{\rm BH}$ ($10^6\,M_\odot$)	$L_{\rm bol}/L_{\rm Edd}$	$M_{\rm BH}$ ($10^6\,M_\odot$)	$L_{\rm bol}/L_{\rm Edd}$	$M_{\rm BH}$ ($10^6\,M_\odot$)	$L_{\rm bol}/L_{\rm Edd}$
This work	$2.50^{+0.29}_{-0.24}$	$0.78^{+0.22}_{-0.21}$	$16.22^{+0.75}_{-0.75}$	$0.12^{+0.03}_{-0.03}$	2.29 ± 2.27[a]	0.85 ± 0.87
Hammerstein et al. (2023)	$2.19^{+0.14}_{-0.00}$	$0.85^{+0.18}_{-0.03}$	$26.91^{+6.81}_{-5.30}$	$0.07^{+0.02}_{-0.02}$	...	...
Hinkle et al. (2021a)	$0.73^{+0.24}_{-0.10}$	$6.75^{+2.23}_{-0.95}$	$7.8^{+3.9}_{-4.1}$	$0.63^{+0.32}_{-0.33}$	~12.59[b]	~0.34
Liu et al. (2022)	...	...	...	...	$23.0^{+13.0}_{-12.0}$[c]	~0.06
Nicholl et al. (2022)	...	...	$5.01^{+0.70}_{-0.81}$	...	...	...

Notes. Eddington ratios are calculated for each source using their respective SMBH masses and peak bolometric luminosities.
[a] Value from Wevers (2020) using the WHT spectrum presented here and the Gültekin et al. (2009b) scaling relation.
[b] Using the SDSS DR14 spectrum and the Gültekin et al. (2009b) scaling relation.
[c] Using the Reines & Volonteri (2015) scaling relation.

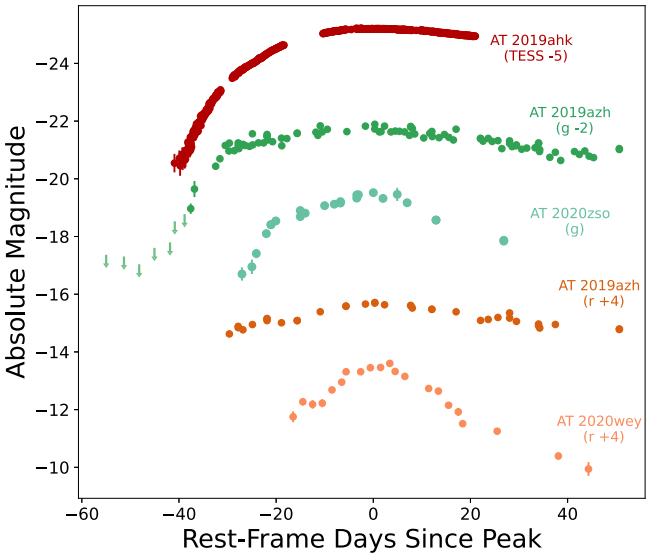

Figure 10. Comparison between the light curves of AT 2019azh (ASAS-SN and Las Cumbres data only, shown for clarity) to those of AT 2019ahk, the TDE with the most densely sampled light curve to date (Holoien et al. 2019b), AT 2020wey (Charalampopoulos et al. 2023), and AT 2020zso. AT 2019ahk lacks any pronounced early-time light-curve structure like that seen in AT 2019azh, despite having high-cadence TESS observations. In contrast, the light curve of the TDE AT 2020wey shows a possible early bump in its *r*-band light curve, and AT 2020zso exhibits a change in its rising slope. Arrows indicate 3σ nondetection upper limits.

Hinkle et al. (2021a) could be due to their use of the pre-corrected UVOT calibrations introduced later by Hinkle et al. (2021b).

4.5. Estimates of the Disrupted Star Mass

The mass derived for the disrupted star also differs substantially between the models, with TDEMass preferring a star roughly 1 order of magnitude more massive than MOSFiT ($4.8^{+4}_{-2.5}$ versus $0.10^{+0.02}_{-0.03}$ $M_\odot$, respectively). In addition to the different model assumptions, this difference could be driven by the MOSFiT prior of a Kroupa initial mass function. Hinkle et al. (2021a) find a similar stellar mass in their MOSFiT fit as in ours, but a much higher one in their TDEMass fit than ours. As mentioned previously, this comparison may not be entirely accurate because of the Swift calibration updates (Hinkle et al. 2021b), not available to Hinkle et al. (2021a), which could influence their bolometric luminosity calculations. Hammerstein et al. (2023) also estimated the stellar mass using these two methods. Our TDEMass-based stellar mass is consistent with their findings, while our MOSFiT-based stellar mass is not. This might be due to differences in the priors used for the efficiency parameter, which is degenerate with the stellar mass. The efficiency parameter inferred from MOSFiT in our analysis is close to the maximum limit of the prior (see Figure C1 in Appendix C). This relatively high efficiency might be additional evidence for contributions to the emission from the stream collision process.

4.6. Self-consistency of MOSFiT Parameters

For the best-fit stellar mass of 0.1 $M_\odot$ and BH mass of $10^{7.21}$ $M_\odot$ given by MOSFiT (see Table 5), assuming $R_\star \approx R_\odot(M_\star/M_\odot) \approx 0.1R_\odot$ (Demircan & Kahraman 1991), the canonical tidal radius is $R_{\rm t} \approx R_\star(M_{\rm BH}/M_\star)^{1/3} \approx 1.6\,GM_{\rm BH}/c^2$. In order to be tidally disrupted and not directly captured by the BH, the tidal radius must be outside of the direct-capture radius (which is larger than the horizon radius for all BH spins $a < 1$, and is $4GM/c^2$ for $a = 0$; e.g., Will 2012). The direct-capture radius is a function of the BH spin, the square of the specific angular momentum of the star, and the projection of the angular momentum onto the spin axis of the BH, and is minimized at a value of[61] $R_{\rm dc} = GM/c^2(1 + \sqrt{1-a})^2$. Requiring that $R_{\rm t} \geqslant R_{\rm dc}$ here sets $a \gtrsim 0.93$ for *any* star to be tidally disrupted and not directly captured. In fact, even with a spin value of $a \approx 1$, it is statistically improbable for the star to be injected into the loss cone, tidally disrupted, and not directly captured; if we assume that stars entering the loss cone are isotropically distributed at large radii and we are in the pinhole regime, such that two-body interactions result in a large relative change in the square of the specific angular momentum of the star on a per orbit basis (e.g., Frank & Rees 1976; Lightman & Shapiro 1977; Merritt 2013; Stone & Metzger 2016), then the formalism described by Coughlin & Nixon (2022) predicts for the parameters here that the fraction of TDEs (i.e., the fraction of stars injected into the loss cone that are tidally disrupted and not directly captured) is ~0.6%. This makes the result highly unlikely.

If the event were a partial TDE, these spin constraints and low probabilities would be somewhat ameliorated. Since a partial TDE occurs at $\sim 2r_{\rm t}$ for a low-mass star (Guillochon & Ramirez-Ruiz 2013; Mainetti et al. 2017; Miles et al. 2020; see

[61] We assume $a > 0$ in this expression, i.e., the stellar angular momentum is aligned with the BH spin (e.g., Will 2012; D'Orazio et al. 2019; Coughlin & Nixon 2022).

also Gafton et al. 2015 in the relativistic case at a comparable BH mass, in particular their Figure 3), the corresponding limit on the BH spin is $a \gtrsim 0.39$. The probability of being tidally disrupted and not directly captured for a BH spin of $a = 0.999$ is then ∼5.1%. Additionally, Coughlin & Nixon (2019) and Miles et al. (2020) found that the fallback rate asymptotically declines as $\propto t^{-9/4}$ (rather than the canonical $t^{-5/3}$) in the case of a partial TDE, which is also more consistent with the best-fit power law of $t^{-2.05}$ for AT 2019azh (assuming that the fallback rate closely tracks the accretion luminosity (e.g., Mockler et al. 2019; Nicholl et al. 2022). However, `MOSFiT` finds a best-fit scaled impact parameter of $b = 0.99^{+0.01}_{-0.03}$, indicating a full disruption. This means that the best-fit $M_{\rm BH}$, $M_\star$, and b from `MOSFiT` are not self-consistent with a fully accretion-powered picture.

Using the extreme upper and lower values for $M_\star$ and $M_{\rm BH}$, respectively, allowed by the total errors listed in Table 5 amealiorates the problem, requiring $a \gtrsim 0.14$ for a full disruption. In addition, if some of the early emission is contributed by outer shocks, this would decrease the rise-time of the accretion-powered part of the light curve, reducing $M_{\rm BH}$ even further, and making a full disruption more likely. We conclude that `MOSFiT` can only marginally fit the data self-consistently assuming a fully accretion-powered light curve, and that at least some contribution from an additional power source at early times is necessary.

If we perform the same calculations using the values from `TDEMass` (i.e., $M_{\rm BH} = 2.5^{+0.29}_{-0.24} \times 10^6\ M_\odot$, $M_\star = 4.8^{+4}_{-2.5}\ M_\odot$), where in this case $R_\star \approx 3R_\odot$ (Demircan & Kahraman 1991), we find $R_{\rm t} \approx 44.3\, GM_{\rm BH}/c^2$. Here, $R_{\rm t} \geqslant R_{\rm dc}$ for any black hole (BH) spin, making this model entirely self-consistent.

4.7. Time Lag between Hα Emission and the Continuum

Our time lag of 1.40 ± 0.93 days between the V-band light curve and Hα luminosity is inconsistent with that of Hinkle et al. (2021a) who measure a ∼23 days time lag. This stems mainly from a difference between our determination of the light-curve peak and theirs. Their light-curve peak was measured at MJD $58548^{+6.30}_{-2.60}$ (roughly 19 days before ours). This peak was determined by Hinkle et al. (2021a) as the median value obtained from fitting a second-order polynomial to 10,000 realizations of bolometric light curves, generated from bolometrically corrected ASAS-SN g-band data, with the bolometric corrections inferred from blackbody fits. The peak light-curve time determined by Hammerstein et al. (2023) of MJD $58566^{+1.16}_{-1.75}$ is closer to ours.

5. Summary and Conclusions

AT 2019azh is a H+He-TDE and is one of the best-observed UV/optical TDEs to date, having extensive spectroscopic coverage and multiwavelength photometric coverage starting several weeks before peak brightness (Figure 1). These observations reveal the following for the first time:

1. A robust change in slope and possible bump in the early light curve of a TDE.
2. The early evolution of the Hα emission line in a TDE.

Unfortunately, no models exist today that can be compared to these observational characteristics; however, they could be used to constrain future models of TDE emission sources and line formation. Relatively high cadence (1–2 days) observations of TDEs are required to test if the light-curve structure observed in AT 2019azh is a common feature of rising TDE light curves.

We detect a possible MIR excess beyond what is expected from the optical/UV blackbody at those wavelengths. This excess, detected 5.15 days after the g-band peak, might be due to a prompt dust echo. However, we are not able to determine its origin without additional observations.

The post-peak bolometric decline of AT 2019azh is not well described by a $t^{-5/3}$ power law, or by any power law, but is better fit by an exponential. We find no significant delay between the peak of the V-band light curve and the Hα luminosity in AT 2019azh.

High-cadence pre-peak observations of more TDEs will be able to determine how common the features seen here are among the TDE population. In addition, more detailed modeling of TDE emission is needed to match the quality of current TDE observations and to help constrain the emission mechanism(s) in TDEs. This is an essential step before we can use TDEs to robustly measure SMBH properties.

Acknowledgments

We thank B. Mockler for helpful advice on using MOSFiT. S.F., I.A., and L.M. acknowledge support from the European Research Council (ERC) under the European Union's Horizon 2020 research and innovation program (grant agreement No. 852097). S.F. and I.A. acknowledge further support from the Israel Science Foundation (grant No. 2108/18). The Las Cumbres Observatory group is supported by National Science Foundation (NSF) grants AST-1911225 and AST-1911151. P.C. and O.G. were supported by the Science & Technology Facilities Council (grants ST/S000550/1 and ST/W001225/1). G.L. was supported by a research grant (19054) from VILLUM FONDEN. M.N. is supported by the ERC under the European Union's Horizon 2020 research and innovation program (grant agreement No. 948381) and by UK Space Agency grant No. ST/Y000692/1. C.P.G. acknowledges financial support from the Secretary of Universities and Research (Government of Catalonia) and by the Horizon 2020 Research and Innovation Program of the European Union under the Marie Skłodowska-Curie program. The SNICE research group acknowledges financial support from the Spanish Ministerio de Ciencia e Innovación (MCIN), the Agencia Estatal de Investigación (AEI) 10.13039/501100011033, and the European Social Fund (ESF) "Investing in your future" under the 2019 Ramón y Cajal program RYC2019-027683-I and the PID2020-115253GA-I00 HOSTFLOWS project, from Centro Superior de Investigaciones Científicas (CSIC) under the PIE project 20215AT016, and the program Unidad de Excelencia María de Maeztu CEX2020-001058-M, and from the Departament de Recerca i Universitats de la Generalitat de Catalunya through the 2021-SGR-01270 grant. S.M. and T.R. acknowledge support from the Research Council of Finland project 350458. A.V.F.'s group at UC Berkeley has been supported by the Christopher R. Redlich Fund, William Draper, Timothy and Melissa Draper, Briggs and Kathleen Wood, Sanford Robertson (T.G.B. is a Draper-Wood-Robertson Specialist in Astronomy), and numerous other donors. F.O. acknowledges support from MIUR, PRIN 2020 (grant 2020KB33TP) "Multimessenger astronomy in the Einstein Telescope Era (METE)." E.R.C. acknowledges support from the National Science Foundation through grant AST-2006684. P.C. acknowledges support via an Academy of

Finland grant (340613; PI: R. Kotak). This work was funded in part by ANID, Millennium Science Initiative, ICN12_009.

This work is based in part on observations collected at the Las Cumbres Observatory, the Copernico 1.82 m Telescope (Asiago Mount Ekar, Italy) operated by the Italian National Astrophysical Institute—INAF, Osservatorio Astronomico di Padova, the European Organization for Astronomical Research in the Southern Hemisphere, Chile, as part of ePESSTO under ESO program ID 199.D-0143(T) (PIs: S. Smartt, C. Inserra), the Nordic Optical Telescope, owned in collaboration by the University of Turku and Aarhus University, and operated jointly by Aarhus University, the University of Turku, and the University of Oslo, representing Denmark, Finland, and Norway, the University of Iceland and Stockholm University at the Observatorio del Roque de los Muchachos, La Palma, Spain, of the Instituto de Astrofisica de Canarias, and on observations made under programme W/2019B/P7 with the William Herschel Telescope operated on the island of La Palma by the Isaac Newton Group of Telescopes in the Spanish Observatorio del Roque de los Muchachos of the Instituto de Astrofísica de Canarias. The NOT observations were obtained through the NUTS Collaboration supported in part by the Instrument Center for Danish Astrophysics (IDA). A major upgrade of the Kast spectrograph on the Shane 3 m telescope at Lick Observatory was made possible through generous gifts from William and Marina Kast as well as the Heising-Simons Foundation. Research at Lick Observatory is partially supported by a generous gift from Google. We thank for their assistance the staff at the various observatories where data were obtained.

This research has made use of the NASA/IPAC Infrared Science Archive, which is funded by the National Aeronautics and Space Administration (NASA) and operated by the California Institute of Technology. This publication also makes use of data products from NEOWISE, which is a project of the Jet Propulsion Laboratory/California Institute of Technology, funded by the Planetary Science Division of NASA. This publication makes use of data products from the WISE, which is a joint project of the University of California, Los Angeles, and the Jet Propulsion Laboratory/California Institute of Technology, funded by NASA.

Supporting research data are available on reasonable request from the corresponding author.

Appendix A
MIR Light Curve

Figure A1 displays the MIR light curves of AT 2019azh. A significant MIR flare appears at 5.15 days after the *g*-band peak.

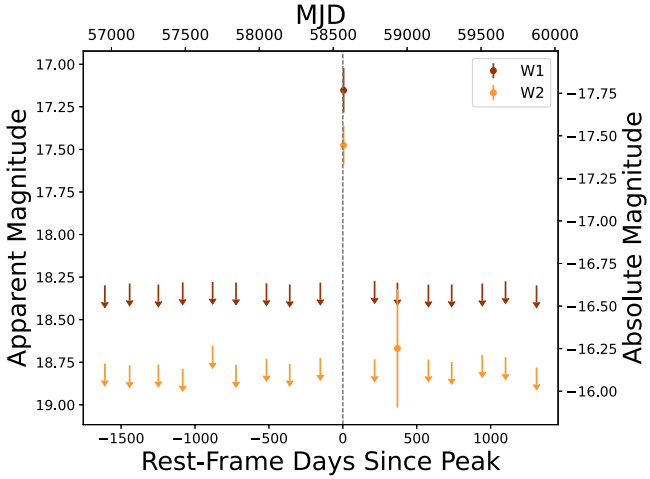

Figure A1. Milky Way extinction-corrected MIR light curves of AT 2019azh from WISE in days relative to the *g*-band peak. Arrows indicate 3σ nondetection upper limits and the dashed vertical line indicates the *g*-band peak.

Appendix B
UV/Optical Peak Fits

Figure B1 displays the second-order polynomial fits around the peak of the light curve for different bands.

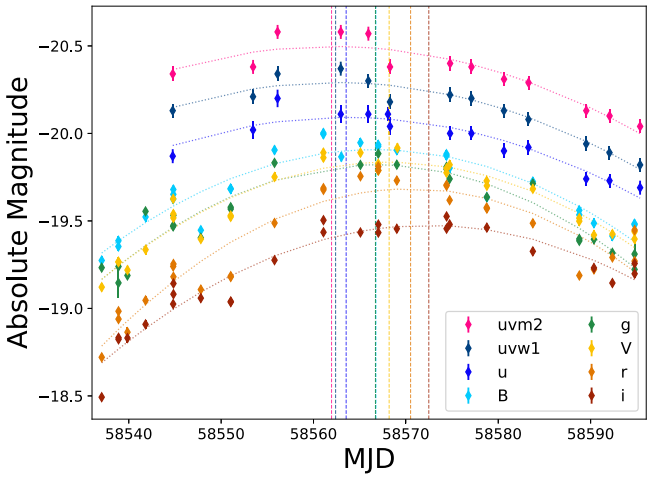

Figure B1. Parabolic fits of the host-subtracted Las Cumbres optical photometry and Swift UV photometry of AT 2019azh around peak brightness. The dashed vertical lines indicate the time of peak for each band from the best-fit parabola.